Inorg. Chem. **2005**, *44*, 4315–4325

Synthesis and Spectroscopic Characterization of a New Family of Ni_4 Spin Clusters

Andreas Sieber,[†] Colette Boskovic,*[,†,‡] Roland Bircher,[†] Oliver Waldmann,[†] Stefan T. Ochsenbein,[†] Grégory Chaboussant,[†,||] Hans U. Güdel,*[,†] Nadeschda Kirchner,[§] Joris van Slageren,*[,§] Wolfgang Wernsdorfer,[#] Antonia Neels,[⊥] Helen Stoeckli-Evans,[⊥] Stefan Janssen,[▽] Fanni Juranyi,[▽,+] and Hannu Mutka[⊗]

Departement für Chemie und Biochemie, Universität Bern, Freiestrasse 3, CH-3012 Bern, Switzerland, School of Chemistry, University of Melbourne, Parkville, Victoria 3010, Australia, Laboratoire Léon Brillouin (LLB-CNRS-CEA), CEA Saclay, 91191 Gif-sur-Yvette Cedex 1, France, 1. Physikalisches Institut, Universität Stuttgart, Pfaffenwaldring 57, 70550 Stuttgart, Germany, Laboratoire L. Néel-CNRS, BP 166, 25 Avenue des Martyrs, 38042 Grenoble Cedex 9, France, Institut de Chimie, Laboratoire de Cristallographie, Université de Neuchâtel, Avenue de Bellevaux 51, CH-2007 Neuchâtel C.P. 2, Switzerland, Paul Scherrer Institut, CH-5232 Villigen, Switzerland, Universität des Saarlandes, Physikalische Chemie, Im Stadtwald, 66123 Saarbrücken, Germany, Institut Laue-Langevin, 6 Rue Jules Horowitz, BP 156, 38042 Grenoble Cedex 9, France

Received January 27, 2005

A new family of tetranuclear Ni complexes $[Ni_4(ROH)_4L_4]$ (H_2L = salicylidene-2-ethanolamine; R = Me (**1**) or Et (**2**)) has been synthesized and studied. Complexes **1** and **2** possess a $[Ni_4O_4]$ core comprising a distorted cubane arrangement. Magnetic susceptibility and inelastic neutron scattering studies indicate a combination of ferromagnetic and antiferromagnetic pairwise exchange interactions between the four Ni^{II} centers, resulting in an $S = 4$ spin ground state. Magnetization measurements reveal an easy-axis-type magnetic anisotropy with $D \approx -0.93$ cm^{-1} for both complexes. Despite the large magnetic anisotropy, no slow relaxation of the magnetization is observed down to 40 mK. To determine the origin of the low-temperature magnetic behavior, the magnetic anisotropy of complex **1** was probed in detail using inelastic neutron scattering and frequency domain magnetic resonance spectroscopy. The spectroscopic studies confirm the easy-axis-type anisotropy and indicate strong transverse interactions. These lead to rapid quantum tunneling of the magnetization, explaining the unexpected absence of slow magnetization relaxation for complex **1**.

Introduction

Single-molecule magnets (SMMs) are clusters that contain a finite number of exchange coupled magnetic centers. An easy-axis-type (Ising) magnetic anisotropy of the spin ground state S splits its M_S components into degenerate $\pm M_S$ sublevels, with $M_S = \pm S$ lowest in energy. This leads to a preferred orientation of the molecular spin S along the easy-axis with an energy barrier between the "up" ($M_S = +S$) and "down" ($M_S = -S$) orientation. For spin reorientation, the spin has to overcome the barrier. This process is no longer possible by thermal activation when the thermal energy is much lower than the barrier. The spin is frozen, and slow relaxation of the magnetization is observed. Furthermore, quantum tunneling of the magnetization through the energy barrier is typically observed in SMMs.[1] SMMs are therefore very interesting candidates for fundamental research into quantum phenomena[2] as well as for potential applications in nanomagnetic devices or quantum computing.[3] The most

* Authors to whom correspondence should be addressed. E-mail: c.boskovic@unimelb.edu.au (C.B.); hans-ulrich.guedel@iac.unibe.ch (H.U.G.); slageren@pi1.physik.uni-stuttgart.de (J.v.S.).
[†] Universität Bern.
[‡] University of Melbourne.
[||] Laboratoire Léon Brillouin.
[§] Universität Stuttgart.
[#] Laboratoire L. Neel-CNRS.
[⊥] Université de Neuchâtel.
[▽] Paul Scherrer Institut.
[+] Universität des Saarlandes.
[⊗] Institut Laue-Langevin.

(1) (a) Thomas, L.; Lionti, F.; Ballou, R.; Gatteschi, D.; Sessoli, R.; Barbara, B. *Nature* **1996**, *383*, 145−147. (b) Friedman, J. R.; Sarachik, M. P.; Tejada, J.; Ziolo, R. *Phys. Rev. Lett.* **1996**, *76*, 3830−3833.
(2) Gatteschi, D.; Sessoli, R. *Angew. Chem., Int. Ed.* **2003**, *42*, 268−297.

10.1021/ic050134j CCC: $30.25
Published on Web 05/10/2005

Scheme 1

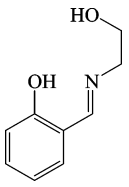

important objective of research in the field of SMMs is the development of an understanding of the relationship between structure, magnetic anisotropy, and observed magnetic behavior.[4−6] Exploitation of these insights will ultimately allow the synthesis of new SMMs that can function at higher temperatures and therefore fulfill their potential in practical applications.

For integer spin systems, the energy barrier between the "up" and "down" spin orientation is $\Delta E = |D|S^2$, where D is the axial zero-field splitting (ZFS) parameter ($D < 0$). To observe slow relaxation phenomena at relatively high temperatures, the cluster should have a large ground-state spin S and a large negative D. The anisotropy of the cluster arises mainly from the anisotropy of the constituent metal centers but depends on their relative orientations.[4,7,8] Thus metals that have a large single-ion anisotropy like Mn^{III} or Ni^{II} are promising candidates for the construction of new SMMs. Most known SMMs contain Mn^{III}, among them is Mn_{12}-acetate for which SMM behavior was first observed.[9] A handful of Ni^{II}-containing SMMs have been reported, including Ni_{12}[10] and Ni_{21}[11] complexes in addition to several Ni_4 complexes with structures based on distorted cubanes.[8,12−14] In all of these clusters, slow magnetic relaxation is only observed at temperatures below 1 K.

The coordination chemistry of the Schiff base proligand H_2L (Scheme 1) has a venerable history, dating back to the days prior to the routine availability of X-ray crystallography for the structural characterization of new complexes.[15] As part of an ongoing investigation of metal complexes possessing derivatives of the Schiff base proligand H_2L (Scheme 1),[16] we have previously communicated the species $[Ni_4(MeOH)_4L_4]$ (**1**), which has a structure based on a distorted cubane.[17,18] Preliminary magnetic measurements have revealed an $S = 4$ ground state and a significant easy-axis-type magnetic anisotropy. Thus the slow magnetization relaxation and quantum tunneling characteristic of SMMs were anticipated for this species. Herein we report the investigation of possible SMM behavior for **1**, together with detailed spectroscopic studies using inelastic neutron scattering and frequency domain magnetic resonance spectroscopy, which were performed in order to elucidate the observed magnetic behavior.

Magnetic inelastic neutron scattering (INS) is a powerful spectroscopic technique for obtaining information about the magnetic anisotropy and the exchange interactions in molecular clusters.[18] The electromagnetic interactions between the magnetic moments of the incident neutrons and those of the sample lead to a transfer of energy and momentum between the neutron and the sample. The observed transitions obey well-defined selection rules and contain information about the magnetic nature of the sample. For INS the selection rules are $\Delta M_S = 0, \pm 1$ and $\Delta S = 0, \pm 1$. The selection rule $\Delta M_S = \pm 1$ allows transitions within an S multiplet ($\Delta S = 0$), probing the anisotropy splitting, whereas the selection rule $\Delta S = \pm 1$ induces transitions between different S states, allowing an exploration of the magnetic exchange interactions. INS has been increasingly used in SMM research, where studies of Mn_{12}-acetate[19], Mn_4,[4,5] Fe_4,[20] and Fe_8[21] SMMs have provided detailed insights into the anisotropy of these species, while the exchange interactions in a Ni_{12} SMM[10] and Mn_{12}-acetate[22] were elucidated by INS. In a number of other spin clusters such as V_{15},[23] Cr_8, [24] and

(3) Leuenberger, M. N.; Loss, D. *Nature* **2001**, *410*, 789−793.
(4) Sieber, A.; Chaboussant, G.; Bircher, R.; Boskovic, C.; Güdel, H. U.; Christou, G.; Mutka, H. *Phys. Rev. B* **2004**, *70*, 172413/1-4.
(5) Andres, H.; Basler, R.; Güdel, H. U.; Aromi, G.; Christou, G.; Buttner, H.; Ruffle, B. *J. Am. Chem. Soc.* **2000**, *122*, 12469−12477.
(6) Waldmann, O.; Koch, R.; Schromm, S.; Schülein, J.; Müller, P.; Bernt, I.; Saalfrank, R. W.; Hampel, F.; Balthes, E. *Inorg. Chem.* **2001**, *40*, 2986−2995.
(7) Gatteschi, D.; Sorace, L. *J. Solid State Chem.* **2001**, *159*, 253−261.
(8) Nakano, M.; Matsubayashi, G. E.; Muramatsu, T.; Kobayashi, T. C.; Amaya, K.; Yoo, J.; Christou, G.; Hendrickson, D. N. *Mol. Cryst. Liq. Cryst. Sci. Technol.* **2002**, *376*, 405−410.
(9) Sessoli, R.; Gatteschi, D.; Caneschi, A.; Novak, M. A. *Nature* **1993**, *365*, 141−143.
(10) Andres, H.; Basler, R.; Blake, A. J.; Cadiou, C.; Chaboussant, G.; Grant, C. M.; Güdel, H. U.; Murrie, M.; Parsons, S.; Paulsen, C.; Semadini, F.; Villar, V.; Wernsdorfer, W.; Winpenny, R. E. P. *Chem. Eur. J.* **2002**, *8*, 4867−4876.
(11) Ochsenbein, S. T.; Murrie, M.; Rusanov, E.; Stoeckli-Evans, H.; Sekine, C.; Güdel, H. U. *Inorg. Chem.* **2002**, *41*, 5133−5140.
(12) Moragues-Canovas, M.; Helliwell, M.; Ricard, L.; Riviere, E.; Wernsdorfer, W.; Brechin, E.; Mallah, T. *Eur. J. Inorg. Chem.* **2004**, 2219−2222.
(13) (a) Yang, E. C.; Wernsdorfer, W.; Hill, S.; Edwards, R. S.; Nakano, M.; Maccagnano, S.; Zakharov, L. N.; Rheingold, A. L.; Christou, G.; Hendrickson, D. N. *Polyhedron* **2003**, *22*, 1727−1733. (b) Edwards, R. S.; Maccagnano, S.; Yang, E. C.; Hill, S.; Wernsdorfer, W.; Hendrickson, D.; Christou, G. *J. Appl. Phys.* **2003**, *93*, 7807−7809.
(14) del Barco, E.; Kent, A. D.; Yang, E. C.; Hendrickson, D. N. *Phys. Rev. Lett.* **2004**, *93*, 157202/1-4.
(15) (a) Yamada, S.; Kuge, Y.; Yamanouc, K. *Bull. Chem. Soc. Jpn.* **1967**, *40*, 1864−1867. (b) van den Bergen, A.; Murray, K. S.; West, B. O.; Buckley, A. N. *J. Chem. Soc. A* **1969**, 2051−2060. (c) Bertrand, J. A.; Breece, J. L.; Kalyanar, Ar; Long, G. J.; Baker, W. A. *J. Am. Chem. Soc.* **1970**, *92*, 5233−5234.
(16) (a) Boskovic, C.; Bircher, R.; Tregenna-Piggott, P. L. W.; Güdel, H. U.; Paulsen, C.; Wernsdorfer, W.; Barra, A. L.; Khatsko, E.; Neels, A.; Stoeckli-Evans, H. *J. Am. Chem. Soc.* **2003**, *125*, 14046−14058. (b) Boskovic, C.; Labat, G.; Neels, A.; Güdel, H. U. *J. Chem. Soc., Dalton Trans.* **2003**, 3671−3672. (c) Boskovic, C.; Sieber, A.; Chaboussant, G.; Güdel, H. U.; Ensling, J.; Wernsdorfer, W.; Neels, A.; Labat, G.; Stoeckli-Evans, H.; Janssen, S. *Inorg. Chem.* **2004**, *43*, 5053−5068.
(17) Boskovic, C.; Rusanov, E.; Stoeckli-Evans, H.; Güdel, H. U. *Inorg. Chem. Commun.* **2002**, *5*, 881−886.
(18) Basler, R.; Boskovic, C.; Chaboussant, G.; Güdel, H. U.; Murrie, M.; Ochsenbein, S. T.; Sieber, A. *Chem. Phys. Chem.* **2003**, *4*, 910−926.
(19) (a) Bircher, R.; Chaboussant, G.; Sieber, A.; Güdel, H. U.; Mutka, H. *Phys. Rev. B* **2004**, *70*, 212413/1-4. (b) Mirebeau, I.; Hennion, M.; Casalta, H.; Andres, H.; Güdel, H. U.; Irodova, A. V.; Caneschi, A. *Phys. Rev. Lett.* **1999**, *83*, 628−631.
(20) Amoretti, G.; Carretta, S.; Caciuffo, R.; Casalta, H.; Cornia, A.; Affronte, M.; Gatteschi, D. *Phys. Rev. B* **2001**, *64*, 104403/1-7.
(21) Caciuffo, R.; Amoretti, G.; Murani, A.; Sessoli, R.; Caneschi, A.; Gatteschi, D. *Phys. Rev. Lett.* **1998**, *81*, 4744−4747.
(22) Chaboussant, G.; Sieber, A.; Ochsenbein, S.; Güdel, H. U.; Murrie, M.; Honecker, A.; Fukushima, N.; Normand, B. *Phys. Rev. B* **2004**, *70*, 104422/1-16.
(23) Chaboussant, G.; Basler, R.; Sieber, A.; Ochsenbein, S. T.; Desmedt, A.; Lechner, R. E.; Telling, M. T. F.; Kögerler, P.; Müller, A.; Güdel, H. U. *Europhys. Lett.* **2002**, *59*, 291−297.

$CsFe_8$[25] the exchange as well as the anisotropy interactions were elucidated by INS.

Frequency domain magnetic resonance spectroscopy (FDMRS) is the frequency domain equivalent of high-frequency EPR; the oscillating magnetic field of the microwave radiation induces magnetic dipole transitions within a spin multiplet ($\Delta M_S = \pm 1$, $\Delta S = 0$) by interaction with the spin angular momentum of the molecule. Because the spectra are recorded in the frequency domain, the experiments can be performed in zero applied field. The observed magnetic dipole transitions give a detailed insight into the anisotropy of the molecule under study.[26] Compared to INS, less information is obtained since $\Delta S = \pm 1$ transitions are not allowed; however, the quantity of sample required for FDMRS is an order of magnitude less than that for INS. In contrast to the standard EPR technique, absolute values of the magnetic susceptibility due to the resonance transitions are straightforwardly obtained. Previous studies have been performed on mononuclear complexes containing integer spin ions with large ZFS[27] as well as on spin clusters such as V_{15} [28] and the SMMs Mn_{12}-acetate[29] and Fe_8.[30]

Experimental Section

Syntheses. All manipulations were performed under aerobic conditions, using materials as received. Salicylidene-2-ethanolamine (H_2L) was prepared as described.[17]

$[Ni_4(MeOH)_4L_4]$ (1). $Ni(OAc)_2 \cdot 4H_2O$ (0.72 g, 2.9 mmol) was added to a solution of H_2L (0.48 g, 2.9 mmol) and NaOH (0.23 g, 5.8 mmol) in MeOH (50 cm^3), affording a green precipitate almost immediately. The precipitate was recrystallized by layering a solution in EtOAc with 2 vol of MeOH; yield 90%. Generally a monoclinic crystal form was isolated (**1a**); however, employment of a very concentrated EtOAc solution resulted in more rapid formation of crystals that were identified as a triclinic crystal form (**1b**). Anal. Calcd for $C_{40}H_{52}N_4Ni_4O_{12}$: C, 47.30; H, 5.16; N, 5.52%. Found: C, 47.15; H, 5.12; N, 5.27%. Selected IR data (cm^{-1}): 1645 (s), 1600 (s), 1539 (m), 1467 (s), 1449 (s), 1393 (m), 1339 (s), 1308 (m), 1226 (w), 1187 (m), 1150 (m), 1127 (m), 1060 (s), 1035 (m), 973 (w), 926 (w), 888 (w), 758 (s), 739 (m), 643 (m), 617 (m), 555 (m), 510 (m), 469 (w), 420 (m).

$[Ni_4(EtOH)_4L_4]$ (2). Complex **2** was synthesized from the same reaction employed for **1**, with the precipitate recrystallized from CH_2Cl_2/EtOH. A sample for crystallography was maintained in contact with mother liquor to prevent the loss of interstitial solvent, and this species was crystallographically identified as **2**$\cdot CH_2Cl_2$. Drying the crystals under vacuum afforded a fully desolvated species that thermogravimetric analysis confirmed was hygroscopic. Anal. Calcd for **2**$\cdot H_2O$ $C_{44}H_{68}N_4Ni_4O_{16}$: C, 46.20; H, 5.99; N, 4.90%. Found: C, 46.14; H, 5.34; N, 4.69%. Selected IR data (cm^{-1}): 1645 (s), 1601 (s), 1537 (m), 1466 (s), 1449 (s), 1388 (m), 1360 (w), 1338 (s), 1308 (m), 1269 (w), 1226 (w), 1185 (m), 1147 (m), 1127 (m), 1092 (m), 1059 (s), 1033 (m), 967 (w), 924 (m), 887 (m), 845 (w), 958 (s), 736 (m), 643 (m), 615 (m), 555 (m), 511 (w), 468 (w), 420 (m).

X-ray Crystallography. The intensity data for single crystals of compounds **1a**, **1b**, and **2**$\cdot CH_2Cl_2$ were collected at 153 K on a Stoe Image Plate Diffraction System[31] using Mo Kα graphite monochromated radiation. Complex **1a** employed: image plate distance 80 mm, ϕ oscillation scans 0−150°, step $\Delta\phi = 1°$, θ range 2.00−23.99°, $d_{max}-d_{min} = 14.23-0.87$ Å. Complex **1b** employed: image plate distance 70 mm, ϕ oscillation scans 0−200°, step $\Delta\phi = 1.5°$, θ range 2.15−25.08°, $d_{max}-d_{min} = 12.45-0.81$ Å. Compound **2** employed: image plate distance 70 mm, ϕ oscillation scans 0−200°, step $\Delta\phi = 1°$, θ range 2.15−25.08°, $d_{max}-d_{min} = 12.45-0.81$ Å. The structures of all three compounds were solved by direct methods using the program SHELXS-97[32] and refined using weighted full-matrix least-squares techniques on F^2. The refinement and all further calculations were carried out using SHELXL-97.[33] Crystallographic data for **1a**, **1b**, and **2**$\cdot CH_2Cl_2$ are given in Table 1.

For all three complexes the OH hydrogen atoms were located from difference Fourier maps and refined isotropically. The remaining H atoms were included in calculated positions and treated as riding atoms using SHELXL-97 default parameters, and the non-H atoms were refined anisotropically. For **1b** and **2**$\cdot CH_2Cl_2$, an empirical absorption correction was applied using DIFABS in PLATON99. Compound **2** crystallizes with two independent molecules of the tetranuclear Ni complex and two CH_2Cl_2 molecules per asymmetric unit. The two coordinated EtOH molecules are disordered, having occupancies of 0.5 for atoms C39, C39a, C40, C40a, C81, and C81a. Both CH_2Cl_2 molecules are disordered over two positions with half occupancy for all atoms.

Magnetic Measurements. Variable temperature magnetic susceptibility measurements down to 1.8 K were performed with a Quantum Design MPMS-XL susceptometer equipped with a 5 T magnet. Data were collected on powdered crystals, restrained in eicosane to prevent torquing and to retard solvent loss from the intact crystals. Pascal's constants were used to estimate the diamagnetic correction for each complex. Low-temperature magnetic measurements were performed on single crystals using an array of micro-SQUIDS.[34] Measurements were performed on this magnetometer in the temperature range 0.04−7.0 K, with fields up to 1.4 T. The experimental susceptibility data were fit using the Levenberg−Marquardt least-squares fitting algorithm, in combination with MAGPACK.[35]

Inelastic Neutron Scattering Measurements. INS experiments were performed on IN5 at the Institut Laue-Langevin (ILL) in

(24) (a) Carretta, S.; van Slageren, J.; Guidi, T.; Liviotti, E.; Mondelli, C.; Rovai, D.; Cornia, A.; Dearden, A. L.; Carsughi, F.; Affronte, M.; Frost, C. D.; Winpenny, R. E. P.; Gatteschi, D.; Amoretti, G.; Caciuffo, R. *Phys. Rev. B* **2003**, *67*, 094405/1-8. (b) Waldmann, O.; Guidi, T.; Carretta, S.; Mondelli, C.; Dearden, A. L. *Phys. Rev. Lett.* **2003**, *91*, 237202/1-4.
(25) Waldmann, O.; Dobe, C.; Mutka, H.; Furrer, A.; Güdel, H. U. Submitted for publication; cond-mat/0410447.
(26) van Slageren, J.; Vongtragool, S.; Gorshunov, B.; Mukhin, A. A.; Karl, N.; Krzystek, J.; Telser, J.; Müller, A.; Sangregorio, C.; Gatteschi, D.; Dressel, M. *Phys. Chem. Chem. Phys.* **2003**, *5*, 3837−3843.
(27) (a) Vongtragool, S.; Gorshunov, B.; Dressel, M.; Krzystek, J.; Eichhorn, D. M.; Telser, J. *Inorg. Chem.* **2003**, *42*, 1788−1790. (b) Rogez, G.; Rebilly, J.-N.; Barra, A. L.; Sorace, L.; Kirchner, N.; Duran, M.; van Slageren, J.; Parsons, S.; Ricard, L.; Marvilliers, A.; Mallah, T. *Angew. Chem., Int. Ed.* (in press).
(28) Vongtragool, S.; Gorshunov, B.; Mukhin, A. A.; van Slageren, J.; Dressel, M.; Müller, A. *Phys. Chem. Chem. Phys.* **2003**, *5*, 2778−2782.
(29) (a) Vongtragool, S.; Mukhin, A.; Gorshunov, B.; Dressel, M. *Phys. Rev. B* **2004**, *69*, 104410/1-5. (b) Dressel, M.; Gorshunov, B.; Rajagopal, K.; Vongtragool, S.; Mukhin, A. A. *Phys. Rev. B* **2003**, *67*, 060405/1-4.
(30) Mukhin, A.; Gorshunov, B.; Dressel, M.; Sangregorio, C.; Gatteschi, D. *Phys. Rev. B* **2001**, *63*, 214411/1-7.
(31) *IPDS Software*; Stoe & Cie GmbH: Darmstadt, Germany, 2000.
(32) Sheldrick, G. M. *Acta Crystallogr.* **1990**, *46*, 467−473.
(33) Sheldrick, G. M. *SHELXL-97*; Universität Göttingen: Göttingen, Germany, 1999.
(34) Wernsdorfer, W. *Adv. Chem. Phys.* **2001**, *118*, 99−190.
(35) Borras-Almenar, J. J.; Clemente-Juan, J. M.; Coronado, E.; Tsukerblat, B. S. *Inorg. Chem.* **1999**, *38*, 6081−6088.

Table 1. Crystallographic Data for **1a**, **1b**, and **2**·CH_2Cl_2

	1a	**1b**	**2**·CH_2Cl_2
formula	$C_{40}H_{52}N_4Ni_4O_{12}$	$C_{40}H_{52}N_4Ni_4O_{12}$	$C_{45}H_{62}Cl_2N_4Ni_4O_{12}$
fw	1015.70	1015.70	1156.73
space group	$P2_1/n$	$P\bar{1}$	$P\bar{1}$
cryst class	monoclinic	triclinic	triclinic
a, Å	13.0750(9)	13.1852(13)	14.5644(12)
b, Å	18.2933(10)	13.6138(13)	14.5954(11)
c, Å	18.7624(13)	14.2325(15)	24.772(2)
α, deg	90	65.582(11)	86.900(10)
β, deg	110.260(7)	75.087(11)	86.347(10)
γ, deg	90	70.346(11)	70.041(9)
V, Å^3	4210.0(5)	2169.8(4)	4936.7(7)
Z	4	2	4
T, K	153(2)	153(2)	153(2)
λ, Å	0.71073	0.71073	0.71073
ρ_{calc}, g cm^{-3}	1.602	1.555	1.556
μ, mm^{-1}	1.828	1.774	1.674
obsd data [$I > 2\sigma(I)$]	5200	5786	14205
R1w[a]	0.0305	0.0455	0.0415
wR2	0.0736[b]	0.1077[c]	0.1035[d]

[a] $R1 = \sum||F_o| - |F_c||/\sum|F_o|$. [b] $wR2 = [\sum w(F_o^2 - F_c^2)^2/\sum wF_o^4]^{1/2}$; $w = 1/[\sigma^2(F_o^2) + (0.0455P)^2]$, where $P = (F_o^2 + 2F_c^2)/3$. [c] $wR2 = [\sum w(F_o^2 - F_c^2)^2/\sum wF_o^4]^{1/2}$; $w = 1/[\sigma^2(F_o^2) + (0.0693P)^2]$, where $P = (F_o^2 + 2F_c^2)/3$. [d] $wR2 = [\sum w(F_o^2 - F_c^2)^2/\sum wF_o^4]^{1/2}$; $w = 1/[\sigma^2(F_o^2) + (0.0563P)^2 + 3.8362P]$, where $P = (F_o^2 + 2F_c^2)/3$.

Grenoble, France, and on FOCUS at the Paul Scherrer Institut (PSI) in Villigen, Switzerland. Spectra were acquired in the temperature range 1.5−22 K on 3 g of an undeuterated, microcrystalline sample of **1a** sealed in a slab-shaped aluminum container with dimensions 3 × 30 × 50 mm^3. On IN5 the spectra were recorded with an incident wavelength $\lambda_i = 8$ Å (fwhm = 0.2 cm^{-1}) in the energy transfer range from −7.5 to 7.5 cm^{-1}. The accessible *Q* range is 0.15−1.4 Å^{-1}. The time-of-flight to energy conversion and the data reduction was done with the standard program INX (ILL). The FOCUS data were measured with an incident wavelength $\lambda_i = 4.75$ Å and inelastic focusing at 9.7 cm^{-1} corresponding to a fwhm = 0.8 cm^{-1}. The energy transfer range is from −25 to 25 cm^{-1} with an accessible *Q* range from 0.23 to 2.4 Å^{-1}. The time-of-flight to energy conversion and the data reduction employed the standard program IDA (TU Munich and PSI). In both experiments the data were corrected for detector efficiency by means of a spectrum of vanadium metal. The data correspond to the sum of all available detectors. Further data treatment included subtraction of the background (approximated by polynomials) and fitting of the observed transitions using Gaussians to extract relative intensities and peak positions.

Frequency Domain Magnetic Resonance Measurements. FDMRS spectra were recorded on a microcrystalline powder pellet (0.314 g; 0.279 cm thick and 1 cm in diameter) of **1a** using linearly polarized radiation. Spectra were acquired in the energy range between 2 and 8 cm^{-1} at 1.8, 5, 10, 20, and 30 K in zero applied magnetic field. The setup of the experiment has been described elsewhere.[26,36]

Other Measurements. Infrared spectra (KBr disk) were recorded on a Perkin-Elmer Spectrum One FTIR spectrometer. Elemental analyses were performed at the Ecole d'Ingénieurs et d'Architectes de Fribourg, Switzerland.

Results

Synthesis. Treatment of a methanolic solution of Na_2L with 1 equiv of $Ni(OAc)_2$ leads to the rapid precipitation of a dark green solid in high yield. This can be recrystallized from EtOAc/MeOH to afford large green crystals of [Ni_4-$(MeOH)_4L_4$] (**1**). Complex **1** crystallizes without solvent of crystallization and can be obtained in either a monoclinic or a triclinic crystallographic form. The nature of the material that is obtained apparently depends on the speed of crystallization. Rapid crystallization affords the triclinic species, suggesting that this is the kinetically favored form, while slower crystallization affords the monoclinic product, which is apparently the thermodynamically favored form. These are indistinguishable by IR spectroscopy but readily distinguished on the basis of their powder X-ray diffraction patterns. Alternatively, recrystallization of the crude product from CH_2Cl_2/EtOH affords large green crystals of [Ni_4-$(EtOH)_4L_4$] (**2**). Once formed, the crystals of both **1** and **2** are completely insoluble and cannot be recrystallized further.

Structure Description. Labeled ORTEP plots of **1a**, **1b**, and **2** are shown in Figure 1, and tables of pertinent structural parameters are available in Supporting Information. A comparison of selected interatomic distances and angles is provided in Table 2.

The structures of **1** and **2** each incorporate a distorted [Ni_4-(μ_3-O)$_4$] cubane core, where the μ_3-O bridges involve the ethoxo-type O atoms of L^{2-}. The L^{2-} ligands coordinate in the typical bis-chelating fashion. The peripheral ligation is completed by four terminal MeOH or EtOH ligands for **1** and **2**, respectively, which participate in intramolecular hydrogen-bonding interactions (O···O distances: 2.62−2.74 Å) with the phenoxo-type O atoms of the L^{2-} ligands, across four of the six faces of the cubane. As a result, these four faces exhibit shorter Ni···Ni separations, smaller Ni−O−Ni angles, and smaller Ni−O−O−Ni dihedral angles (Table 2). In addition, **1** and **2** appear to possess a slight tetragonal elongation of the Ni coordination, which occurs along the O−Ni−O vector involving the ROH and trans alkoxo ligands, with Ni−O (L^{2-}-ethoxo) bonds on this vector of 2.11−2.15 Å versus 2.02−2.05 Å for the "equatorial" Ni−O (L^{2-}-ethoxo) bonds. Thus, the complexes display approximate S_4 point symmetry, while the exact crystallographic

(36) Kozlov, G. V.; Volkov, A. A. *Coherent Source Submillimeter Wave Spectroscopy*; Springer: Berlin, 1998.

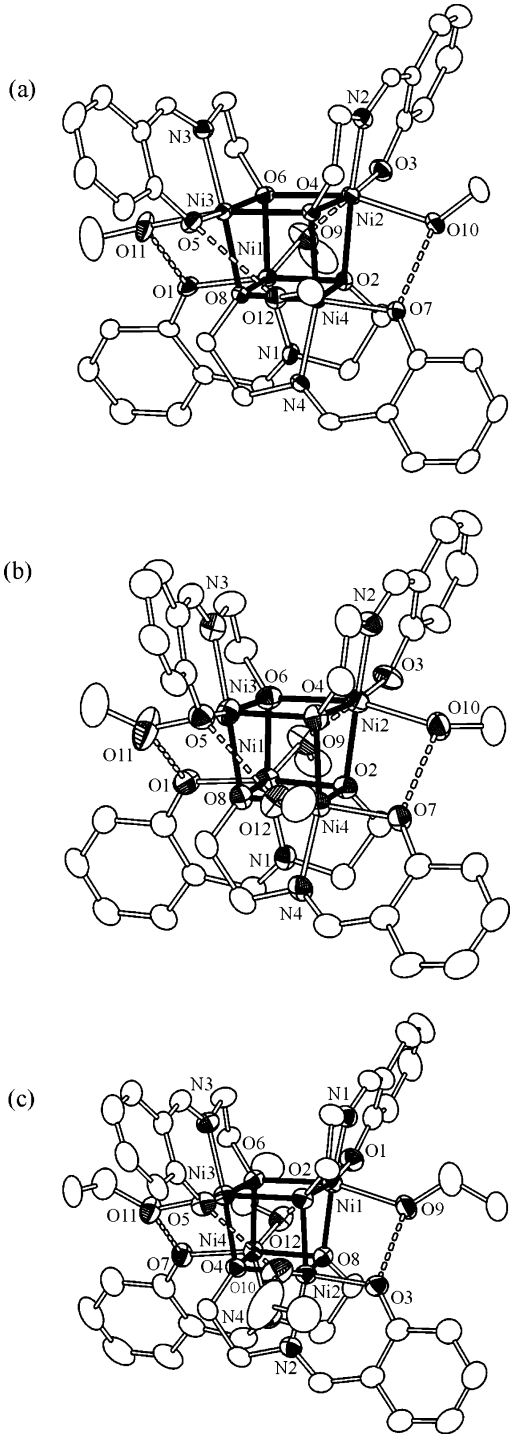

Figure 1. Ortep representations at the 50% probability level of (a) complex **1a**, (b) complex **1b**, and (c) one of the independent molecules of complex **2** in **2**·CH_2Cl_2.

point symmetry is C_1. No significant differences are observed between the two crystallographically independent molecules present in **2**·CH_2Cl_2. Moreover, it is noteworthy that in the solid-state structures for each of the three compounds, the Ni_4 molecules are canted with respect to each other, affording two different orientations of the cubane units. The approximate S_4 axes are canted by about 50°. In each structure, the individual Ni_4 molecules can be considered to be well isolated with closest intermolecular Ni···Ni separations of 6.9, 6.9, and 8.0 Å for **1a**, **1b**, and **2**·CH_2Cl_2, respectively.

Table 2. Selected Interatomic Distances (Å) and Angles (deg) for **1a**, **1b**, and **2**·CH_2Cl_2

parameter	**1a**	**1b**	**2**·CH_2Cl_2
Ni···Ni[a]	3.03−3.04	3.03−3.04	3.03−3.05
Ni···Ni[b]	3.18−3.20	3.20−3.21	3.20−3.21
Ni−O[c]	2.02−2.05	2.02−2.05	2.02−2.05
Ni−O[d]	2.11−2.14	2.11−2.13	2.11−2.15
O···O[e]	2.62−2.72	2.67−2.74	2.66−2.74
Ni−O−Ni[a]	93.1−97.4	93.3−97.4	92.7−97.2
Ni−O−Ni[b]	100.1−101.2	100.5−101.8	100.5−101.6
Ni−O−O−Ni[a]	165−166	164−166	164−166
Ni−O−O−Ni[b]	178−180	178−180	179−180

[a] Across the four hydrogen-bonded faces. [b] Across the two non-hydrogen-bonded faces. [c] "Equatorial" L^{2-}-ethoxo. [d] "Elongated" L^{2-}-ethoxo. [e] O−H···O.

In addition, there are no obvious intermolecular hydrogen bonds.

Several Ni^{II}_4 complexes with similar cubane structures have been reported previously, including examples with equivalent intramolecular hydrogen-bonding interactions; although, a tetragonal elongation is not evident in these complexes.[12,37] However, Oshio and co-workers[38] have also reported a tetragonal elongation of the Ni coordination in the structure of complex **1a**, in addition to the complex $[Fe_4(MeOH)_4L_4]$, which possesses a similar tetragonal elongation of the Fe^{II} coordination.[39] An equivalent distortion is also evident in the structurally related species $[Cu_4L_4]$.[40] This suggests that, within the cubane arrangement that is observed for divalent transition metal ions with the ligand L^{2-}, the steric requirements of the ligand induce a distortion of the metal coordination.

Magnetic Studies. Variable temperature DC susceptibility measurements were performed at 0.1 T on a collection of intact small crystals of **1a**, **1b**, and **2**·H_2O, in the temperature range 1.8−300 K. The data are plotted in Figure 2 as $\chi_M T$ and χ_M versus T. For each of the samples, the value of $\chi_M T$ increases progressively from a value of ≈5.1 $cm^3\ mol^{-1}$ K at 300 K to ≈11.4 $cm^3\ mol^{-1}$ K at ≈7.5 K before rapidly decreasing to ≈9.4 $cm^3\ mol^{-1}$ K at 1.8 K. The spin-only value of $\chi_M T$ for four noninteracting Ni^{II} centers is 4.4 $cm^3\ mol^{-1}$ K ($g = 2.2$) and the behavior is consistent with overall ferromagnetic intramolecular interactions. The data for the three samples were fit to the exchange Hamiltonian

$$\hat{H}_{ex} = -2J_A(\hat{S}_1\cdot\hat{S}_4 + \hat{S}_2\cdot\hat{S}_3) - 2J_B(\hat{S}_1\cdot\hat{S}_2 + \hat{S}_1\cdot\hat{S}_3 + \hat{S}_2\cdot\hat{S}_4 + \hat{S}_3\cdot\hat{S}_4) \quad (1)$$

above 20 K, where J_A characterizes exchange across the two

(37) (a) Murray, K. S. *Adv. Inorg. Chem.* **1995**, *43*, 261−358. (b) Halcrow, M. A.; Sun, J. S.; Huffman, J. C.; Christou, G. *Inorg. Chem.* **1995**, *34*, 4167−4177. (c) ElFallah, M. S.; Rentschler, E.; Caneschi, A.; Gatteschi, D. *Inorg. Chim. Acta* **1996**, *247*, 231−235. (d) Escuer, A.; Font-Bardia, M.; Kumar, S. B.; Solans, X.; Vicente, R. *Polyhedron* **1999**, *18*, 909−914. (e) Mukherjee, S.; Weyhermüller, T.; Bothe, E.; Wieghardt, K.; Chaudhuri, P. *Eur. J. Inorg. Chem.* **2003**, 863−875. (f) Clemente-Juan, J. M.; Chansou, B.; Donnadieu, B.; Tuchagues, J. P. *Inorg. Chem.* **2000**, *39*, 5515−5519.

(38) Nihei, M.; Hoshino, N.; Ito, T.; Oshio, H. *Polyhedron* **2003**, *22*, 2359−2362.

(39) (a) Oshio, H.; Hoshino, N.; Ito, T. *J. Am. Chem. Soc.* **2000**, *122*, 12602-12603. (b) Oshio, H.; Hoshino, N.; Ito, T.; Nakano, M. *J. Am. Chem. Soc.* **2004**, *126*, 8805−8812.

Table 3. Derived Spin Hamiltonian Parameters for **1a**, **1b**, and **2**·H_2O

measure[a]		**1a**		**1b**		**2**·H_2O	
susceptibility	g	2.18(2)	2.19(3)	2.23(4)	2.25(5)	2.20(2)	2.20(2)
	J_A (cm^{-1})	−3.5(8)	8.7(8)	−3(1)	8(1)	−2.9(3)	8.1(3)
	J_B (cm^{-1})	8.8(6)	1.6(3)	8(1)	1.5(4)	7.8(3)	1.5(1)
magnetization	g	2.19(5)		2.19(3)		2.25(6)	
	D (cm^{-1})	−0.94(7)		−0.93(6)		−1.0(1)	

[a] Simulations or fits performed as described in the text.

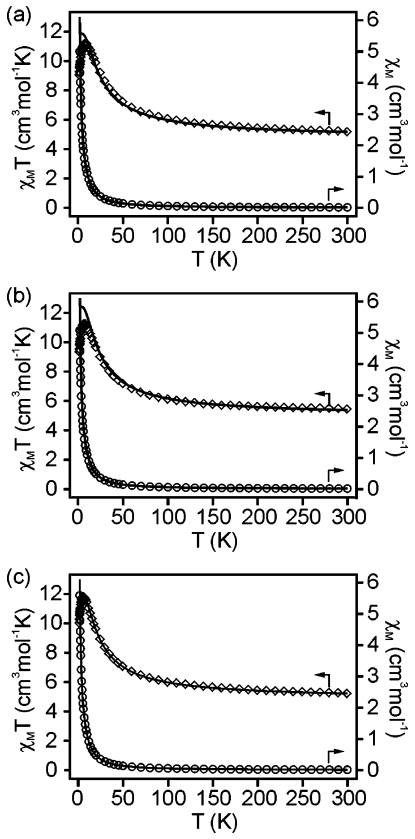

Figure 2. Plot of χ_M and $\chi_M T$ vs T measured in a 0.1 T field for (a) **1a**, (b) **1b**, and (c) **2**·H_2O. The solid lines represent the best fits of the data between 300 and 20 K to eq 1 as described in the text.

Scheme 2

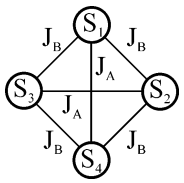

faces of the Ni_4 cubane that are not bridged by hydrogen bonds, while J_B characterizes the remaining four pairwise interactions (Scheme 2). This yielded two sets of parameters for each compound (Table 3), which gave equally good fits to the experimental data. The data below 20 K were excluded from the fit, with the sharp decrease in $\chi_M T$ at low temperatures consistent with the effects of ZFS and/or antiferromagnetic intermolecular interactions. The g values of ≈2.2 are consistent with those typically observed for Ni^{II}. The average values for the three compounds were as follows: $J_A = -3(1)$ cm^{-1}, $J_B = 8(1)$ cm^{-1}, $g = 2.22(5)$ and $J_A = 8(1)$ cm^{-1}, $J_B = 1.5(4)$ cm^{-1}, $g = 2.23(7)$. From magnetization measurements, the $S = 4$ ground state was derived (vide infra). As both parameter sets result in a spin ground state of $S = 4$, the maximum possible for a Ni^{II}_4 species, they cannot be distinguished by this criterion. The first set of fitting parameters is preferred as it is in better agreement with the previously reported correlation between coupling constants and structural parameters. The study of a number of Ni_4 complexes with distorted cubane structures and bridging O atoms has revealed that the observed exchange interactions between Ni centers make a transition from ferromagnetic to antiferromagnetic as the Ni−O−Ni bridging angles increase above ≈98° and the Ni−O−O−Ni dihedral angles increase above ≈170°.[37] Thus for the present complexes, the four hydrogen-bonded faces of the cubane (characterized by J_B) display angles typical for ferromagnetic interactions (Table 2), while the remaining two faces (characterized by J_A) possess angles consistent with antiferromagnetic exchange interactions. This favors the first set of exchange coupling constants (see Table 3).

Variable temperature magnetization measurements were performed on the three compounds in the temperature range 1.8−8 K, with fields up to 5 T. The data are presented in Figure 3 as plots of $M/N\mu_B$ versus H/T. For all three species $M/N\mu_B$ values of ≈7.6 were obtained at 5 T and 1.8 K and clearly indicate $S = 4$ ground states. It was possible to simulate the data for the three compounds using the ZFS Hamiltonian

$$\hat{H}_{ZFS} = D\left[\hat{S}_z^{\,2} - \frac{1}{3}S(S+1)\right] \qquad (3)$$

assuming axial anisotropy and a well-isolated $S = 4$ ground state. The simulations for all three compounds reproduce the data very well over the full field and temperature range used. The simulation parameters are given in Table 3. It should be noted that it was not possible to obtain a good simulation of the data with $D > 0$.

The $S = 4$ and $D \approx -1$ cm^{-1} values suggest that **1** and **2** should have an anisotropy barrier to magnetization reversal of $|D|S^2 \approx 16$ cm^{-1} (23 K). This is potentially large enough for the manifestation of slow relaxation of the magnetization at low temperature, and thus low-temperature magnetization measurements were performed on single crystals of **1a** down to 0.04 K using a micro-SQUID apparatus. Figure 4 shows magnetization versus field measurements at a sweep rate of 0.07 T s^{-1} and different temperatures in the range 0.04−7.0 K, with the magnetization normalized to the saturation value M_{sat}. The magnetic field is applied at an angle of 25° with

(40) Chumakov, Y. M.; Biyushkin, V. N.; Malinovskii, T. I.; Kulemu, S.; Tsapkov, V. I.; Popov, M. S.; Samus, N. M. *Koord. Khim.* **1990**, *16*, 945−949.

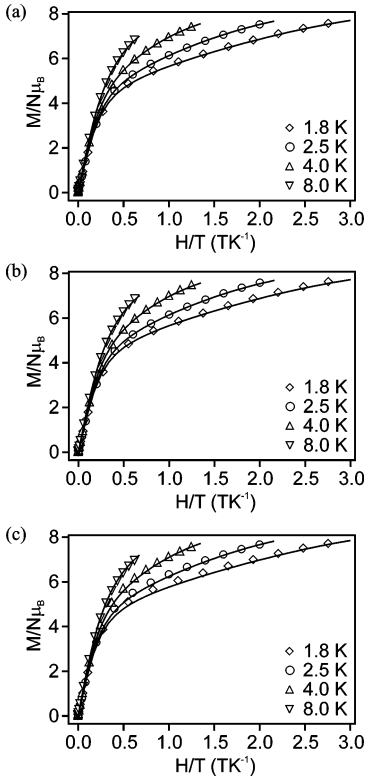

Figure 3. Plot of $M/N\mu_B$ vs H/T for (a) **1a**, (b) **1b**, and (c) **2**·H_2O. The solid lines represent the simulations as described in the text.

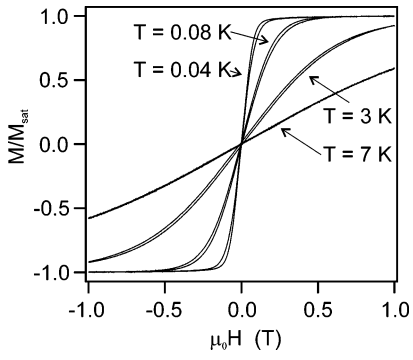

Figure 4. Plot of magnetization (M) (normalized to its saturation value M_{sat}) vs applied field for a single crystal of **1a**.

respect to the cluster anisotropy axis (approximate S_4 axis). This is due to the fact, that the cubane units have two different orientations within the unit cell. A slight butterfly-like hysteresis is seen in the data, which is characteristic of a phonon-bottleneck, whereby the phonon exchange (thermal coupling) between the crystal and its environment is retarded, hampering the spin relaxation. Such a phenomenon has been previously observed in V_{15}[41] and $NaFe_6$.[42] However, for **1a** no true hysteresis arising from the molecular anisotropy-induced energy barrier of the molecule was observed.

Inelastic Neutron Scattering. Despite the fact that the INS experiments were performed on an undeuterated sample of **1a**, excellent spectra were obtained, showing a large number of well-resolved peaks. Figure 5 shows the INS

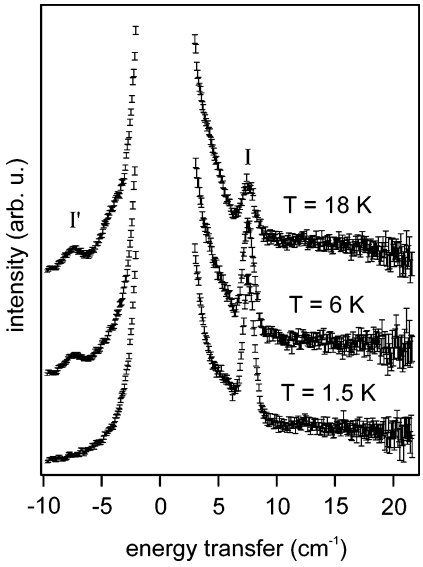

Figure 5. INS spectra at 1.5, 6, and 18 K of a polycrystalline sample of **1a** recorded on FOCUS with an incident wavelength $\lambda_i = 4.75$ Å. The spectra correspond to the sum of all the scattering angles. The labeling of the peaks corresponds to Figure 10 and Table 4.

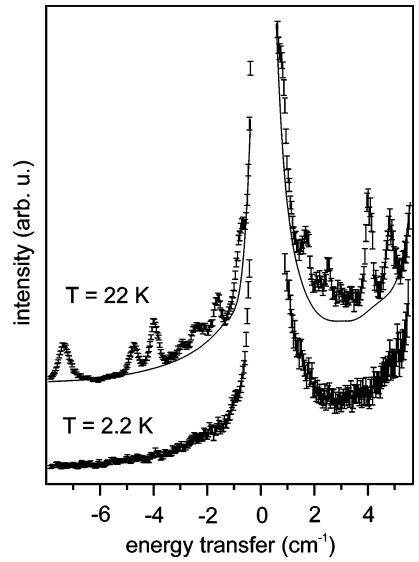

Figure 6. INS spectra at 2.2 and 22 K of a polycrystalline sample of **1a** recorded on IN5 with an incident wavelength $\lambda_i = 8$ Å. The spectra correspond to the sum of all the scattering angles. The solid line represents the background.

spectra of a polycrystalline sample of **1a** at three different temperatures measured on FOCUS. At 1.5 K one cold transition (I) at 7.4 cm^{-1} on the neutron energy loss side is observed. At elevated temperatures its intensity decreases and the corresponding transition (I′) is observed on the gain side. Furthermore, some hot intensity is found in the energy region below transition I. No peaks are observed between 10 and 22 cm^{-1}. The low energy region was studied in detail with higher resolution on IN5. Figure 6 shows the data at 2.2 and 22 K. No inelastic peaks are observed at 2.2 K. At 22 K seven peaks on the loss side and eight peaks on the gain side are observed. The solid line in Figure 6 represents the experimental background as derived from the 2 K data, which does not exhibit magnetic excitations, and the data after background subtraction are given in Figure 7. The

(41) Chiorescu, I.; Wernsdorfer, W.; Müller, A.; Bogge, H.; Barbara, B. *Phys. Rev. Lett.* **2000**, *84*, 3454−3457.
(42) Waldmann, O.; Koch, R.; Schromm, S.; Müller, P.; Bernt, I.; Saalfrank, R. W. *Phys. Rev. Lett.* **2002**, *89*, 246401/1-4.

Table 4. Calculated and Experimental FDMRS and INS Transitions for Compound **1a**

		FDMRS		INS		relative intensity at 22 K			
		energy (cm^{-1})		energy (cm^{-1})		loss side		gain side	
label	transition[a]	exp	calcd[b]	exp	calcd[b]	exp[c]	calcd[b]	exp[c]	calcd[b]
I	$\|4\rangle_{A,S} \leftrightarrow \|3\rangle_{A,S}$	7.33(2)	7.35	7.37(4)	7.35			0.81	1.01
II	$\|3\rangle_{A,S} \leftrightarrow \|2\rangle_{A}$	4.80(8)	4.80	4.77(8)	4.80	0.71	0.79	0.59	0.59
III	$\|3\rangle_{A,S} \leftrightarrow \|2\rangle_{S}$	4.00(8)	4.01	4.01(8)	4.01	0.94	0.98	0.80	0.76
IV	$\|2\rangle_{S} \leftrightarrow \|1\rangle_{S}$			2.92(8)	2.90	0.15	0.32	0.29	0.28
V	$\|2\rangle_{S} \leftrightarrow \|1\rangle_{A}$			2.50(8)	2.49	0.45	0.51	0.35	0.45
VI	$\|2\rangle_{A} \leftrightarrow \|1\rangle_{S}$			2.18(8)	2.11	0.26	0.46	0.31	0.41
VII	$\|2\rangle_{A} \leftrightarrow \|1\rangle_{A}$			1.67(8)	1.70	0.73	0.50	0.62	0.45
VIII	$\|1\rangle_{A} \leftrightarrow \|0\rangle$			0.82(8)	0.91	1.00	0.80	1.00	0.77

[a] Labeling of the transitions is given in Figure 10. [b] Calculations were performed as described in the text using eqs 3−5 and the parameter values in Table 5. [c] Intensities were normalized to 1 for transition VIII for both the loss and gain side.

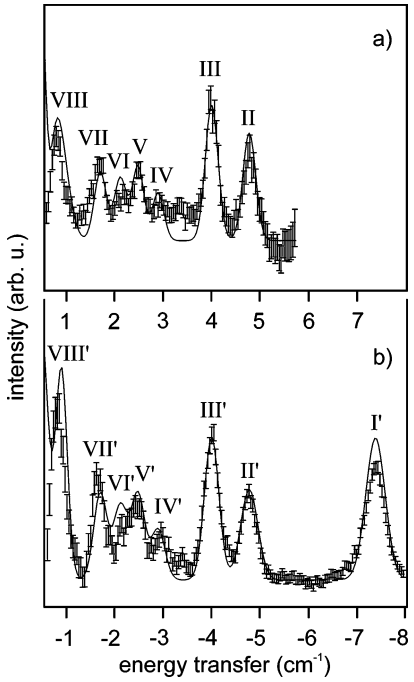

Figure 7. INS spectra at 22 K of a polycrystalline sample of **1a** recorded on IN5 with an incident wavelength $\lambda_i = 8$ Å after background subtraction: (a) energy loss side, (b) energy gain side. The labeling of the peaks corresponds to Figure 10 and Table 4. The solid line represents the calculated spectra using the parameters given in Table 5. Different scaling factors were used for the loss and gain side.

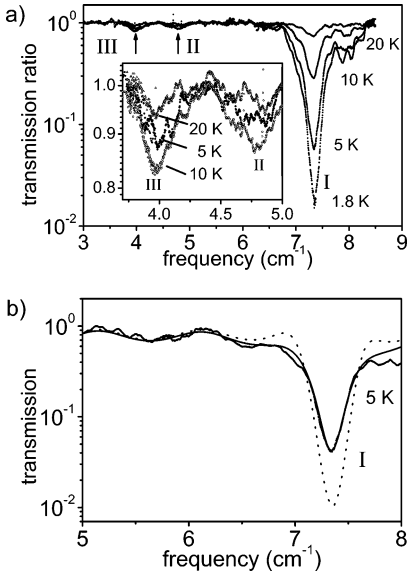

Figure 8. (a) Normalized FDMRS spectra of **1a** at 1.8, 5, 10, and 20 K. The data are divided by the spectra taken at 30 K. The labeling of the peaks corresponds to Figure 6 and Table 4. The inset shows an enlargement of transitions II and III. (b) Raw FDMRS data and calculated spectra of transition I at $T = 5$ K using Lorentzian (solid line) and Gaussian (dotted line) line shapes.

energy positions and the relative intensities of the transitions were extracted from the data using Gaussians and are listed in Table 4. The peaks are about a factor of 2 broader than the instrumental resolution. Transition I′, for example, has a fwhm = 0.47 cm^{-1}, whereas the instrumental resolution at this energy transfer is 0.28 cm^{-1}.

Frequency Domain Magnetic Resonance Spectroscopy. Figure 8a shows the FDMRS spectra obtained at 1.8, 5, 10, and 20 K on a polycrystalline sample of **1a** after normalization involving division by the 30 K data; and Figure 8b shows the raw 5 K FDMRS data. In the raw FDMRS data, an oscillating and temperature-independent baseline caused by the interference of the radiation between the parallel surfaces of the sample is present. After normalization by the 30 K data, which removes this baseline, three narrow, temperature-dependent absorption lines are visible, which are associated with allowed $\Delta M_S = \pm 1$ magnetic dipole transitions within the ground-state multiplet ($\Delta S = 0$). At 1.8 K a strong transition (I) is observed at 7.3 cm^{-1}. At elevated temperature its intensity decreases and two less intense transitions II and III appear at 4.8 and 4.0 cm^{-1}. The positions of the transitions are determined by a high degree polynomial fit and are given in Table 4. The temperature dependence of the resonance intensities of transitions I−III is given in Figure 9. Note that these are absolute intensities.

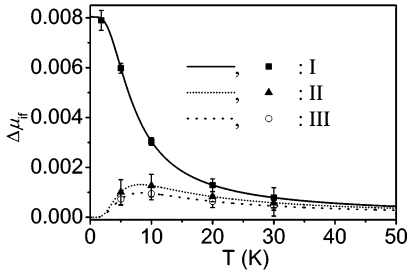

Figure 9. Temperature dependence of the absolute resonance intensities of the FDMRS transitions I−III of **1a**. The lines represent the calculated intensities using eq 5b and the parameter values given in Table 5.

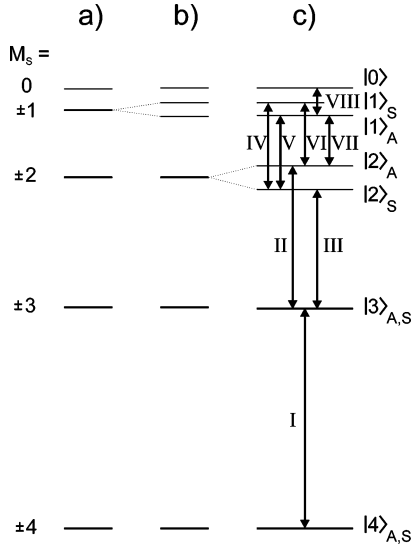

Figure 10. Zero-field splitting of the $S = 4$ ground state of **1a** using the parameters given in Table 5. (a) First two terms of eq 3. (b) Including the E term in eq 3. (c) Including B_4^4 in eq 3. The double arrows show the observed transitions.

Analysis of INS and FDMRS Spectra. The anisotropy splitting of the $S = 4$ ground state of **1a** can be expressed using the following Hamiltonian:

$$\hat{H}_{\text{aniso}} = D\left[\hat{S}_z^2 - \frac{1}{3}S(S+1)\right] + B_4^0\hat{O}_4^0 + E(\hat{S}_x^2 - \hat{S}_y^2) + B_4^4\hat{O}_4^4 \quad (4)$$

$$\hat{O}_4^0 = 35\hat{S}_z^4 - 30S(S+1)\hat{S}_z^2 + 25\hat{S}_z^2 - 6S(S+1) + 3S^2(S+1)^2 \text{ and } \hat{O}_4^4 = \frac{1}{3}(\hat{S}_+^4 + \hat{S}_-^4)$$

As a result of the axial D and B_4^0 terms, the $S = 4$ ground-state splits in zero field into five degenerate $\pm M_S$ sublevels, with $M_S = \pm 4$ lowest in energy (Figure 10a). The E term represents the rhombic anisotropy, and as seen is Figure 10b, its main effect is to remove the degeneracy of the $M_S = \pm 1$ sublevels (in principle the E term connects states with $\Delta M_S = \pm 2$ but in first-order of perturbation theory only a splitting of the $M_S = \pm 1$ is induced). The E term in **1a** arises from distortions of strict S_4 cluster symmetry. Since Ni^{II} ($S = 1$) cannot afford a fourth or higher order single-ion anisotropy contribution, the cluster anisotropy B_4^4 term is caused by the mixing of higher lying $S = 3$ and $S = 2$ states into the $S = 4$ ground state.[43] The B_4^4 term mixes M_S functions differing by ± 4; its main effect is to split the $M_S = \pm 2$ levels (in first-order of perturbation theory), see Figure 10c. With respect to the wave functions, these observations imply that the new eigenstates are well approximated by the symmetric and antisymmetric linear combinations of the respective M_S functions, labeled in Figure 10c as $|M_S\rangle_S$ and $|M_S\rangle_A$, respectively. On the basis of the $\Delta M_S = \pm 1$ selection rule, nine transition are expected within the $S = 4$ ground state in the INS as well as in the FDMRS spectra. Eight of these are observed in the INS experiments and three are observed in the FDMRS experiment. The agreement between INS and FDMRS data is excellent. From the observed transitions an energy level diagram can be constructed as shown in Figure 10c. The observed transitions are displayed as double arrows. Transitions I to III are assigned considering their temperature dependence (Figure 9), whereas the others are assigned on the basis of their energy differences. The anisotropy parameters are determined from the data by fitting the eigenvalues of eq 3 to the observed energies. The result of the fitting and the parameter values are given in Tables 4 and 5, respectively. The agreement of $D = -0.93(2)$ cm^{-1} with the value $D = -0.94(7)$ cm^{-1} derived from magnetization measurements (Table 3) is excellent. It was found that all the higher order terms are essential to fully interpret the data (i.e., inclusion of each of them significantly improves the fit).

Table 5. ZFS Parameter for **1a** Derived from INS and FDMRS Data

D	−0.93(2) cm^{-1}
B_4^0	−0.00043(16) cm^{-1}
$\|E\|$	0.023(8) cm^{-1}
B_4^4	−0.0021(4) cm^{-1}

For an isolated $S = 4$ state the magnetic INS intensity between an initial state $|i\rangle$ and a final state $|f\rangle$ is proportional to $|\langle f|\hat{S}_\perp|i\rangle|^2$, where $\hat{S}_\perp$ is the spin component perpendicular to the scattering vector $\mathbf{Q} = \mathbf{k_i} - \mathbf{k_f}$ ($\mathbf{k_i}$ and $\mathbf{k_f}$ are the initial and final wavevectors). The scattering intensity is proportional to the correlation function $S(\mathbf{Q}, \hbar\omega)$, which after averaging over all orientations of $\mathbf{Q}$ (polycrystalline sample), is given by eq 4:[44]

$$S(\mathbf{Q},\hbar\omega) = f^2(\mathbf{Q}) \times \sum_{i,f} p_i \frac{1}{3}(2|\langle f|\hat{S}_z|i\rangle|^2 + |\langle f|\hat{S}_+|i\rangle|^2 + |\langle f|\hat{S}_-|i\rangle|^2)\delta(\hbar\omega - (E_f - E_i)) \quad (4)$$

$$p_i = \exp(-E_i/k_BT)/\sum_i \exp(-E_i/k_BT)$$

p_i is the Boltzmann factor of the level i, and the delta function is convoluted by the experimental resolution function. $f(\mathbf{Q})$ is the magnetic form factor. The experimental and calculated transition energies as well as their normalized intensities are given in Table 4. The calculated INS spectra are shown as solid lines in Figure 7. Different scaling factors were used for the loss and gain side. The overall agreement between experiment and calculation is very good.

The FDMRS spectra can be calculated using the frequency dispersion of the complex dielectric permittivity (ϵ) and the magnetic permeability (μ) together with the Fresnel formulas for the transmission of a plane parallel layer. The baseline oscillations are governed by the temperature independent complex dielectric permittivity; they are fitted at high temperatures where no resonance lines are observable. The imaginary part of the magnetic permeability describes the power absorbed during the induced magnetic dipole transi-

(43) (a) Stevens, K. W. H. Spin Hamiltonians. In *Magnetism*; Rado, G. T., Suhl, H., Eds.; Academic Press: New York, 1963; Vol. I. (b) Carretta, S.; Liviotti, E.; Magnani, N.; Amoretti, G. *J. Appl. Phys.* **2003**, *93*, 7822−7824.

(44) Birgenau, R. J. *J. Phys. Chem. Solids* **1972**, *33*, 59−68.

tions and therefore the intensity of the experimentally observed absorption lines. The frequency dispersion of the magnetic permeability is expressed as follows:

$$\mu = 1 + \sum_{i,f} \Delta\mu_{if} R(\omega) \tag{5a}$$

where $R(\omega)$ is the line shape function (Gaussian or Lorentzian) and $\Delta\mu_{if}$ denotes the absolute resonance intensity of the transition between $|i\rangle$ and $|f\rangle$ state as given by eq 5b within the single-spin approximation:

$$\Delta\mu_{if} = \frac{8\pi}{3}\frac{N_A}{M_r}\rho\frac{g^2\mu_B{}^2\sum_{\alpha=x,y,z}|\langle f|\hat{S}_\alpha|i\rangle|^2}{\hbar\omega_{fi}}(p_i - p_f) \tag{5b}$$

with the Boltzmann factor p_i and p_f defined as in eq 4. $\rho(N_A/M_r)$ is the concentration of paramagnetic ions with ρ being the density of the sample, N_A is the Avogadro constant, and M_r is the molecular weight. Finally, $\hbar\omega_{fi}$ is the resonance energy.

The spectra were calculated with the parameters given in Table 5 and $g = 2.19$. A Lorentzian line shape with a temperature independent fwhm $= 0.33$ cm^{-1} was used. It is not possible to simulate the data using a Gaussian line shape (see Figure 8b). The agreement with the experiment is very good, especially when taking into consideration that no scaling is involved, and only the line width is taken as a fit parameter.

In addition to information about the magnetic anisotropy, information about the magnetic exchange interactions can also be obtained from the INS spectra, as the INS selection rule $\Delta S = \pm 1$ allows transitions between different S multiplets. For molecule **1a** two sets of coupling parameters are derived from the magnetic susceptibility data (vide supra). For the first set of parameters ($J_A = -3.5(8)$ cm^{-1}, $J_B = 8.8(6)$ cm^{-1}) all the $\Delta S = \pm 1$ transitions are expected at energies greater than 22 cm^{-1}, whereas for the second set of parameters ($J_A = 8.7(8)$ cm^{-1}, $J_B = 1.6(3)$ cm^{-1}) a cold transition at $\approx$19 cm^{-1} and a hot transition at $\approx$13 cm^{-1} are expected. No magnetic INS intensity is observed in the region between 10 and 22 cm^{-1} (Figure 5), verifying the first set of parameters.

Discussion

From the parameters given in Table 5 an energy difference between the $M_S = 0$ and $M_S = \pm 4$ levels of 14.8(4) cm^{-1} is calculated for molecule **1a**. This barrier is larger than the 7 cm^{-1} [12] and 10−11 cm^{-1} [13] barriers calculated for the structurally similar Ni_4 complexes $[Ni_4(thme)_4(MeCN)_4](NO_3)_4$ (H_3thme = 1,1,1-tris(hydroxymethyl)ethane) and $[Ni_4(hmp)_4(ROH)_4Cl_4]$ (Hhmp = 2-hydroxymethylpyridine; R = Me, Et, or ^{t}BuEt), respectively (calculated as $\Delta E = |D|S^2$). These other complexes are all SMMs; thus, SMM behavior may be anticipated for **1a**, based on its larger Ising-type magnetic anisotropy and resulting energy barrier. Nevertheless no slow magnetic relaxation is observed for **1a** down to 40 mK. Notably, the other Ni_4 SMMs show large relaxation steps in their hysteresis at zero field. This is due to fast quantum tunneling of the magnetization and indicates higher-order terms, which lead to some mixing of the M_S basis functions.[12,13] In **1a** we find that both the E and $B_4{}^4$ terms in the anisotropy Hamiltonian are substantial and evidently larger than in the other Ni_4 cluster. As a consequence, the tunneling rates become large enough to preclude the observation of hysteresis even at 40 mK (Figure 4). The applied transverse field in the micro-SQUID experiments, arising from the different orientation of the applied magnetic field with respect to the cluster anisotropy axis (approximate S_4 axis), is much too small to significantly influence the tunneling at zero field.

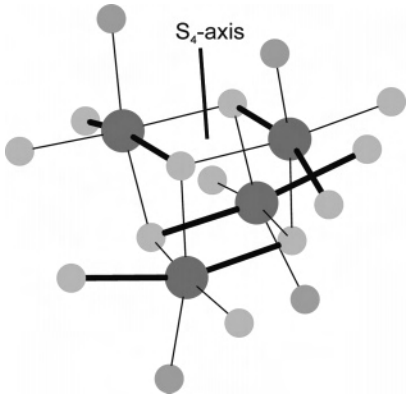

Figure 11. Arrangement of the elongated O−Ni−O bonds (thick lines) of molecules **1** and **2** with respect to the approximate S_4 cluster anisotropy axis. Ni^{II}: dark gray; N: medium gray; O: light gray.

The magnetic anisotropy of a cluster arises mainly from the single-ion anisotropy and the dipole-dipole interactions between the magnetic centers. In the strong-exchange limit, the cluster anisotropy tensor $\check{D}$ is related to the single-ion anisotropy tensors $\check{D}_i$ of the individual Ni^{II} ions by eq 6:[45]

$$\check{D} = \sum_i d_i \check{D}_i + \sum_{i<j} d_{ij} \check{D}_{ij} \tag{6}$$

where d_i are the vector coupling coefficients and $\check{D}_{ij}$ are the contributions arising from dipole-dipole interaction. In the present case the latter are about an order of magnitude weaker than the single-ion contributions[4] and can be neglected. **1** and **2** possess a slight tetragonal elongation of the four Ni coordinations (Figure 1 and Table 2). In octahedral Ni^{II} mononuclear complexes, a positive D parameter is often associated with a weakening of the axial bonds (elongated octahedron), increasing in magnitude with increasing axial elongation.[46] Thus a positive single-ion D with the hard axis along the elongated O−Ni−O bonds can be assumed for all the Ni^{II} centers in **1** and **2**. These single-ion hard axes are approximately perpendicular to the pseudo-S_4 axis of the cluster, and they are pairwise perpendicular to each other (Figure 11). Under the assumption of S_4 cluster point symmetry, eq 6 is transformed into eq 7

$$D = -\frac{1}{14} D_{Ni^{II}} \tag{7}$$

(45) Bencini, A.; Gatteschi, D. *EPR of Exchange Coupled Systems*; Springer-Verlag: Berlin, 1990.

where D is the axial anisotropy parameter of the cluster and $D_{Ni^{II}}$ is the single-ion anisotropy parameter of the Ni^{II} ions. Thus, the particular arrangement of the hard axes of the Ni^{II} ions (positive $D_{Ni^{II}}$) results in an easy-axis-type magnetic anisotropy (negative D) of the molecules of **1** and **2**, as observed experimentally. Negative molecular D values have also been observed for other Ni^{II}_4 clusters with similar cubane-based structures.[8] Using eq 7 and the $D = -0.93$ cm^{-1} value determined in this study, a $D_{Ni^{II}} = 13$ cm^{-1} value can be calculated, which is at the upper limit of the known values for six-coordinate Ni^{II} ions.[46]

In the FDMRS experiment, the highest frequency resonance has a Lorentzian line shape, whereas in the INS experiment Gaussian lines are observed. The observed line shape in the INS experiment is a convolution of the instrumental resolution (Gaussian line shape) and the Lorentzian line shape of the observed transition. Thus, when the Lorentzian width is about the same as the Gaussian width, a Voigt line shape will result. Indeed, transition I′ can be equally well-described using a Voigt function with a Gaussian fwhm $= 0.28$ cm^{-1} (resolution of IN5) and a Lorentzian fwhm $= 0.30$ cm^{-1} instead of a Gaussian with a fwhm $= 0.47$ cm^{-1}. This shows that the FDMRS and INS data are consistent, and it explains why the INS transitions appear broader than expected from the instrumental resolution. The observation of a Lorentzian line shape with a fwhm $= 0.33$ cm^{-1} in the FDMRS experiment is remarkable. Usually Gaussian line shapes with smaller widths are observed in spin clusters. For example in Mn_{12}-acetate, transitions with a fwhm of about 0.2 cm^{-1} [47] are observed, which is two-thirds of that for **1a**. In cases such as Mn_{12}-acetate, the line width is determined by the distribution in D associated with the distribution in molecular structures. The Lorentzian line shape of **1a** is lifetime limited. Apparently in **1a** an intrinsic mechanism is present, which is much faster than in the other SMMs. It is tempting to associate this with the fact that no slow relaxation was observed. This issue is currently under further investigation.

(46) Boca, R. *Coord. Chem. Rev.* **2004**, *248*, 757−815.

Conclusions

A new family of tetranuclear Ni complexes has been synthesized and studied. All complexes have an $S = 4$ ground state and an easy-axis-type magnetic anisotropy. Despite the large magnetic anisotropy, no slow relaxation of the magnetization was observed down to 40 mK. Detailed INS and FDMRS studies on molecule **1a** reveal significant transverse interactions. This opens a pathway for quantum tunneling leading to rapid relaxation of the magnetization.

Acknowledgment. This work was funded by the Swiss National Science Foundation (NFP 47), the German Science Foundation DFG, and the European Union (TMR Quemolna MRTN-CT-2003-504880).

Supporting Information Available: X-ray crystallographic files in CIF format for **1a**, **1b**, and **2**; tables of selected interatomic distances and angles for **1a**, **1b**, and **2** (Tables S1−S3). This material is available free of charge via the Internet at http://pubs.acs.org.

IC050134J

(47) Vongtragool, S.; van Slageren, J.; Gorshunov, B.; Mukhin, A.; Dressel, M. Manuscript in preparation.